Institute of Paper Science and Technology
Atlanta, Georgia

IPST TECHNICAL PAPER SERIES

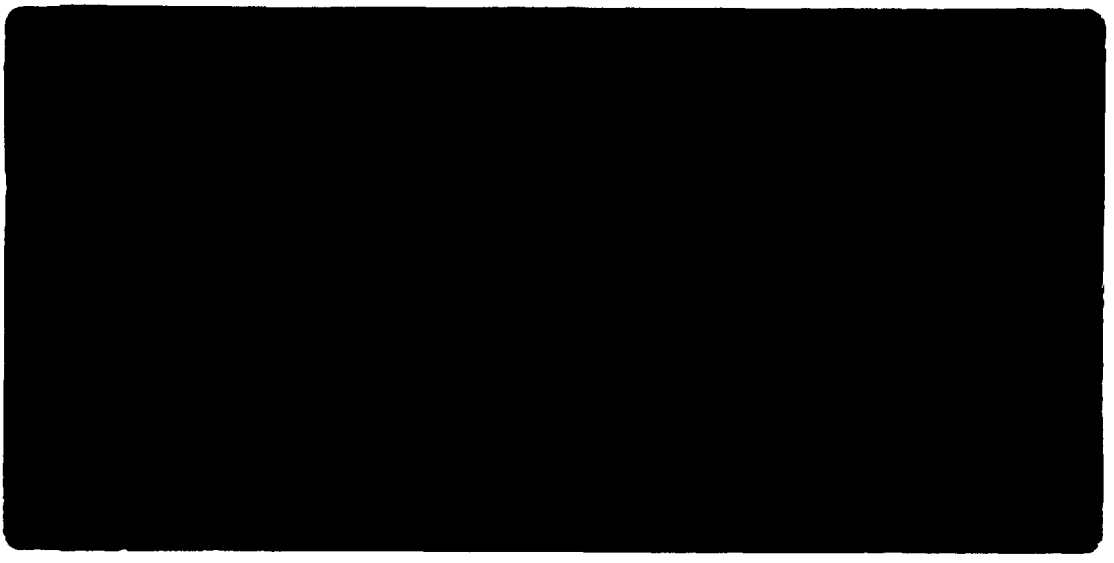

NUMBER 490

A VOLUME-OF-FLUID COMPUTATIONAL TECHNIQUE FOR FREE SURFACE FLOW PROBLEMS

J.F. MC KIBBEN AND C.K. AIDUN

JUNE 1993

A Volume-of-fluid Computational Technique for Free Surface Flow Problems

J.F. McKibben ad C.K. Aidun

Submitted to
J. of Comput. Physics

A VOLUME-OF-FLUID COMPUTATIONAL TECHNIQUE FOR FREE SURFACE FLOW PROBLEMS

John F. McKibben
Doctoral Candidate
Institute of Paper Science and Technology
500 10th Street N.W.
Atlanta, GA 30318

Cyrus K. Aidun
Associate Professor
Institute of Paper Science and Technology
and Department of Mechanical Engineering
Georgia Institute of Technology
500 10th Street N.W.
Atlanta, GA 30318

KEYWORDS

Volume-of-fluid, Thin film stability, Free Surface flows

ABSTRACT

The Volume of Fluid (VOF) method is a simple and robust technique for simulating free surface flows with large deformations and intersecting free surfaces. Earlier implementations used Laplace's equation for the normal stress boundary condition at the interface between the liquid and vapor phases. We have expanded the interfacial boundary conditions to include the viscous component of the normal stress in the liquid phase and, in a limited manner, to allow the pressure in the vapor phase to vary. Included are sample computations that show the accuracy of added third order accurate differencing schemes for the convective terms in the Navier-Stokes equations (NSE), the viscous terms in the normal stress at the interface, and the solution of potential flow in the vapor phase coupled with the solution of the NSE in the liquid phase. With these modifications we show that the VOF method can accurately predict the instability of a thin viscous sheet flowing through a stagnant vapor phase.

I. INTRODUCTION

Current techniques for computational analysis of free surface flows include primarily Lagrangian and Eulerian approaches. In this article we discuss the advantages and disadvantages of both viewpoints. Furthermore, we present an Eulerian approach with advantages in a broad class of free surface flow problems with large surface deformations. Finally, we present results of several test problems which show the possible accuracy with these refinements.

In the Lagrangian approach, the computational mesh is allowed to deform with the surface. This has the distinct advantage of allowing an edge of the computational domain to coincide with the location of the interface, improving the accuracy and simplifying the numerical implementation of the interfacial boundary conditions. Unfortunately, Lagrangian techniques have the disadvantage that, for flows with large surface deformation, the mesh can become distorted or entangled, leading to loss of numerical accuracy and stability [1]. Hirt et al. [2] present an example of a purely Lagrangian approach where the vertices of the computational grid move freely with the local fluid velocity.

In an effort to overcome the grid distortion problem, free Lagrangian approaches have been developed [3,4,5,6]. In these methods, the conserved properties are associated with points that are free to move with fluid. The computational grid is reconstructed at each time step by choosing the nearest neighbors, and the mass and momentum are transferred using the resulting computational grid.

An alternative to the free Lagrangian approach for overcoming the problem of grid distortion is to allow periodic rezoning of the computational grid. This process maintains the integrity of the computational grid while allowing the interface to continue to be represented by the edge of the computational domain. The rezoning process has the side

effect of introducing numerical diffusion as the information is transferred from the old computational grid to the new one. Examples of numerical techniques using rezoning techniques can be found in Hirt et al. [7], Amsden et al. [8], Addesio et al. [9], and Bach and Hassager [10].

In the Eulerian approach, the computational mesh generally remains fixed or is allowed to move in a prescribed manner, while the fluid moves relative to the mesh. Typically, this is accomplished by either introducing some means of tracking interface location [11,12,13,14] or by tracking the location of the fluid itself, referred to as volume tracking [15,16].

The interface tracking methods allow a more accurate representation of the interface, but are generally difficult to extend to three dimensions and complex intersecting flows (e.g., wave breaking) [1]. The volume tracking techniques use localized reconstruction algorithms to identify the interface location and shape. Examples of reconstruction techniques include those used in the volume of fluid (VOF) family of methods [16,17] and the simple line interface calculation (SLIC) [18].

Recently, a modification to the VOF approach has been developed which yields a more accurate representation of the surface tension component of the interfacial boundary condition [19,20,21]. In this approach, termed the continuum surface force (CSF), the surface tension force is spread over a region near the interface with dimensions on the order of the cell spacing. The resulting force is then incorporated as an additional body force in the solution of the flow equations.

Regardless of the method used to track the location of the interface, the equations to be solved for isothermal, incompressible flow are the continuity equation,

$$\nabla \cdot \mathbf{v} = 0, \tag{1}$$

and the Navier-Stokes equation (NSE),

$$\frac{\partial \mathbf{v}}{\partial t} + \mathbf{v} \cdot \nabla \mathbf{v} = \mathbf{g} - \frac{1}{\rho} \nabla P + \nu \nabla^2 \mathbf{v}, \tag{2}$$

where $\mathbf{v}$ is the velocity vector, $\mathbf{g}$ is a body force vector, P is the pressure, ρ is the density, and ν is the kinematic viscosity. These equations are solved, subject to boundary conditions at the edges of the computational domain, along interior obstacles, and at the interface between the liquid and vapor phases.

The interfacial boundary conditions are derived from velocity and stress balances at the interface and continuity of velocity. We begin the definition of the stress balances by defining a localized auxiliary function for the location of the interface,

$$H(x,y) \equiv y - \eta(x) = 0. \tag{3}$$

The surface normal, $\mathbf{n} = (n_x, n_y)$, is computed from gradient of $H(x,y)$, which leads to the unit normal vector:

$$n_x = -\eta'\left(\eta'^2 + 1\right)^{-1/2}, \; n_y = \left(\eta'^2 + 1\right)^{-1/2}, \tag{4}$$

where $\eta' = \partial\eta/\partial x$. The unit tangential, $\mathbf{t} = (t_x, t_y)$, vector may then be computed from the orthogonality condition

$$t_x = \left(\eta'^2 + 1\right)^{-1/2}, \; t_y = \eta'\left(\eta'^2 + 1\right)^{-1/2}. \tag{5}$$

Finally, the surface curvature, κ, is given by,

$$\kappa = \eta''\left(\eta'^2 + 1\right)^{-3/2}. \tag{6}$$

With these definitions in mind and the assumption of an inviscid vapor phase, the boundary conditions at the interface arising from the normal and tangential stress balances are

$$P_\ell - \mathbf{n} \cdot \tau_\ell \cdot \mathbf{n} = P_v - \sigma k \tag{7}$$

and

$$\mathbf{t} \cdot \tau_\ell \cdot \mathbf{n} = 0, \tag{8}$$

respectively, where subscripts ℓ and v refer to the liquid and vapor phases, respectively, σ is the surface tension, and

$$\tau = \mu\left(\frac{\partial v_i}{\partial x_j} + \frac{\partial v_j}{\partial x_i}\right) \tag{9}$$

is the stress tensor. The remaining boundary condition at the interface is due to continuity of normal velocity given by

$$\mathbf{v}_\ell \cdot \mathbf{n} = \mathbf{v}_v \cdot \mathbf{n}. \tag{10}$$

Since the vapor phase is assumed to be inviscid, continuity of the tangential component of velocity cannot be imposed.

In our work, we have chosen to use one of the volume tracking techniques to retain the advantages of simplicity in treating flows with large deformations and folding free surfaces. In order to increase the range of problems which can be accurately studied with this technique, we have extended the SOLA-VOF method to include the viscous terms in the interfacial boundary condition and, in a limited manner, allowed flow of the vapor phase. As we will show below, the consideration of the vapor phase flow and variations in pressure are critically important for stability analysis.

The VOF method is derived from the first generally successful volume tracking free surface program, the Marker and Cell (MAC) method [15]. The MAC method tracks the location of the fluid within a fixed Eulerian mesh through the use of massless marker particles. These particles are convected through the computational domain at the end of each time step using the interpolated local fluid velocity. The free surface is constructed from the cells partially filled with marker particles and having neighboring empty cells. In the MAC method, the normal stress boundary condition at the interface is simplified to

$$p_\ell = p_v. \tag{11}$$

This simplified boundary condition, applied at the cell center rather than at the actual interface location, greatly reduced the accuracy of the computational technique.

The MAC method has evolved into the VOF technique, which can be looked upon as the limit when the number of marker particles becomes infinite. Thus, the liquid is tracked by a step function, F, representing the fraction of each computational cell occupied by liquid. Transport of F through the computational mesh is governed by the F-convection equation,

$$\frac{\partial F}{\partial t} = \mathbf{v} \cdot \nabla F, \tag{12}$$

which ensures that the amount of each phase is conserved.

The interface between the phases is determined on a cellwise basis from local F values. Cells with F = 1 are liquid cells, cells with F = 0 are vapor cells, and cells with intermediate values of F are free surface cells. Once the free surface cells have been identified, the location and shape of the interface within the free surface cells may be reconstructed from gradients of the F function.

The original VOF implementation, SOLA-VOF [17], included the effects of surface tension yielding Laplace's formula

$$P_\ell = P_v - \sigma\kappa \tag{13}$$

as the free surface boundary condition. In addition, the SOLA-VOF technique incorporates an interpolation scheme for applying the boundary condition at the free surface location rather than at the center of the computational cell. Improvements in algorithms for computing surface curvature and methods for treating obstacles within the computational domain were incorporated into the subsequent NASA-VOF2D [22] program. Extension to three dimensions for cylindrical coordinates led to the NASA-VOF3D [23] program. However, all three of these programs neglect the viscous component of the liquid normal stress in the liquid phase at the interface and assume that the pressure in the vapor phase remains constant. These assumptions impose severe

limitations on the applicability of this method to free surface problems where viscous stresses are important.

In the study of free surface flows such as the die-swell problem, inclusion of the viscous terms in the interfacial boundary condition is vital [13,14]. Therefore, implementations which neglect these components are unable to accurately solve this problem. In addition, in the study of the stability of thin liquid films, the viscous terms at the interface and variations in the vapor phase pressure along the interface are the primary factors inducing instability and wave formation [24].

For these reasons, we extend the VOF technique to allow inclusion of the viscous terms in the liquid phase at the interface to allow variation of the pressure in the vapor phase and greatly extend the applicability of the VOF method to free surface problems. We will outline the various solution algorithms, followed by numerical treatment of the static contact line and implementation of viscous components at the interface. Next, the numerical solution of the vapor phase flow, coupled with the liquid phase solution, will be presented, followed by a comprehensive examination of the technique's accuracy.

We solve the lid-driven cavity to examine the accuracy of the solution of the Navier-Stokes equations. The die-swell problem is solved to test the implementation of the viscous stresses at the interface. Finally, we solve for the stability of a liquid sheet and compare the results with those of linear stability analysis. We accurately compute the growth rate of waves in a thin liquid sheet in agreement with predictions from linear stability analysis. The above test problems are solved to demonstrate that, despite popular perception, this method can be very accurate and reliable when the complete interfacial condition is considered.

II. NUMERICAL TECHNIQUE

We begin the description of the numerical technique with a brief outline of the solution algorithm employed in the SOLA family of programs. This is followed by a description of the additions we have made to improve the accuracy and extend the capabilities of our program, IPST-VOF3D. Specifically, we highlight more accurate methods for differencing the convective terms in the NSE, modifications needed to treat a static contact point on an interior obstacle, inclusion of the viscous terms in the liquid at the interface, and solution of the potential flow equations in the vapor phase to yield the pressure in the vapor phase.

A. SOLA Solution Algorithm

In the SOLA family of programs, the velocity and pressure fields are solved on a staggered grid (figure 1). In this representation, vector quantities are stored on cell faces, and scalar quantities at the cell centers.

Here, we briefly describe the numerical method used to solve the NSE in the SOLA family of programs. Generally, this can be described by defining an explicit guess,

$$\tilde{\mathbf{v}}^n = \mathbf{v}^n + \delta t\left[\mathbf{g} - \frac{1}{\rho}\nabla P^n + \nu\nabla^2\mathbf{v}^n - \mathbf{v}^n\cdot\nabla\mathbf{v}^n\right], \tag{14}$$

for the new velocity field, where the superscript refers to the time step. Except as described below for the convective terms, the specifics of the finite difference representations used can be found in Refs. [22], [23], and [25]. The velocity field after the time step can then be written as the explicit guess plus a correction term due to the pressure change across the time step,

$$\mathbf{v}^{n+1} = \tilde{\mathbf{v}}^{n} - \frac{\delta t}{\rho}\nabla\left(\delta P^{n+1}\right). \tag{15}$$

Since mass must be conserved at all times, we may substitute (15) into (1) yielding

$$\frac{\delta t}{\rho} V \nabla\cdot\left[\nabla\left(\delta P^{n+1}\right)\right] = V \nabla\cdot\tilde{\mathbf{v}}^{n}, \tag{16}$$

where V is the volume of the computational cell, needed to ensure a symmetric system of equations [22]. The Poisson equation for pressure, (16), yields a sparse, symmetric linear system of equations that can be solved using a variety of numerical methods such as the successive over-relaxation (SOR) or Conjugate Residual (CR) methods [23]. With the new pressure field available, the updated velocity field is then computed from (15).

The F-convection equation, (12), is solved using donor-acceptor differencing [23] to assist in maintaining a sharp interface between the liquid and the vapor phases. Once the new fluid configuration has been obtained, it is possible to reconstruct the localized interface configuration needed for computation of surface tension force [23]. Again, the details of this process are presented elsewhere [22,23,25].

B. Differencing of the Convective Term

As we will show below, as the Reynolds number increases, the accuracy of the finite difference representation of the convective terms in the NSE limits the accuracy of the entire solution. Therefore, in addition to the standard differencing for the convective terms present in the SOLA programs, we apply and evaluate three third order accurate differencing options: Quadratic Upstream Interpolation for Convective Kinematics (QUICK) [26,27], third order accurate upwind differencing (THIRD) [28,25], and the method of Kawamura and Kuwahara (KANDK) [29,25].

As an example, we define the constant grid formulas for the convective term involving the x-component of velocity in the x-direction,

$$\left(u\frac{\partial u}{\partial x}\right)_{i+1/2}. \tag{17}$$

Analogous formulas have been developed for the remaining terms and, except as noted, for grids with variable cell spacing. Presentation of these formulas and their derivations can be found in Ref. [25].

The first technique, used in the SOLA family of programs, consists of a linear combination of first order accurate upwind differencing and second order accurate central differencing. This leads to the constant grid formulas

$$\left(u\frac{\partial u}{\partial x}\right)_{i+1/2} = \frac{u_{i+1/2}}{2\Delta x}\left[(1+\alpha)u_{i+3/2} - 2\alpha u_{i+1/2} - (1-\alpha)u_{i-1/2}\right] \quad u_{i+1/2} > 0 \tag{18a}$$

and

$$\left(u\frac{\partial u}{\partial x}\right)_{i+1/2} = \frac{u_{i+1/2}}{2\Delta x}\left[(1-\alpha)u_{i+3/2} + 2\alpha u_{i+1/2} - (1+\alpha)u_{i-1/2}\right] \quad u_{i+1/2} < 0, \tag{18b}$$

where Δx is the cell spacing and α controls the fraction of central differencing. Setting $\alpha = 1$ yields first order accurate upwind differencing and setting $\alpha = 0$ yields second order accurate central differencing. Numerical stability considerations limit the fraction of central differencing [23].

The first of the three third order accurate differencing schemes is based on the QUICK differencing technique which uses quadratic upstream interpolation to compute the value of the convected variable at each face of a control volume [26]. These interpolated values are then used to form a centered finite difference formula. We have combined simplified forms of QUICK interpolation formulas [27] to yield the finite difference formulas

$$\left(u\frac{\partial u}{\partial x}\right)_{i+1/2} = \frac{u_{i+1/2}}{8\Delta x}\left(3u_{i+3/2} + 3u_{i+1/2} - 7u_{i-1/2} + u_{i-3/2}\right) \quad u_{i+1/2} > 0 \tag{19a}$$

and

$$\left(u\frac{\partial u}{\partial x}\right)_{i+1/2} = \frac{u_{i+1/2}}{8\Delta x}\left(-u_{i+5/2} + 7u_{i+3/2} - 3u_{i+1/2} - 3u_{i-1/2}\right) \quad u_{i+1/2} < 0 \tag{19b}$$

for our implementation of the QUICK differencing.

The second of the third order accurate differencing techniques, THIRD, was derived for constant grids by Agarwal [28]. This technique again uses upstream differencing for stability, but is derived in a different manner [25]. The finite difference formulas for constant grid spacing are

$$\left(u\frac{\partial u}{\partial x}\right)_{i+1/2} = \frac{u_{i+1/2}}{6\Delta x}\left(2u_{i+3/2} + 3u_{i+1/2} - 6u_{i-1/2} + u_{i-3/2}\right) \qquad u_{i+1/2} > 0 \qquad (20a)$$

and

$$\left(u\frac{\partial u}{\partial x}\right)_{i+1/2} = \frac{u_{i+1/2}}{6\Delta x}\left(-u_{i+5/2} + 6u_{i+3/2} - 3u_{i+1/2} - 2u_{i-1/2}\right) \qquad u_{i+1/2} < 0. \qquad (20b)$$

The final third order accurate technique, termed KANDK, is a differencing scheme developed by Kawamura and Kuwahara [29]. They used an alternative approach to derive a third order accurate scheme, beginning with a second order accurate upwind scheme and eliminating the term leading to the third order error. The constant grid formulas for KANDK are

$$\left(u\frac{\partial u}{\partial x}\right)_{i+1/2} = \frac{u_{i+1/2}}{6\Delta x}\left(u_{i+5/2} - 2u_{i+3/2} + 9u_{i+1/2} - 10u_{i-1/2} + 2u_{i-3/2}\right) \qquad u_{i+1/2} > 0 \quad (21a)$$

and

$$\left(u\frac{\partial u}{\partial x}\right)_{i+1/2} = \frac{u_{i+1/2}}{6\Delta x}\left(-2u_{i+5/2} + 10u_{i+3/2} - 9u_{i+1/2} + 2u_{i-1/2} - u_{i-3/2}\right) \qquad u_{i+1/2} < 0. \quad (21b)$$

A variable grid derivation in the manner used by Kawamura and Kuwahara is not possible. We have modified and extended this third order accurate differencing scheme for variable grids. The derivation is presented in the appendix and other details are reported elsewhere [25].

C. Treatment of a Static Contact Line

Many free surface problems have a contact point or line which join the liquid, vapor, and solid phases. A static contact is the intersection between vapor, liquid, and solid phases where the point of contact is fixed, but the contact angle can vary. The variation

in the contact angle is part of the solution and often has significant effect on the free surface shape. An example is the die-swell problem described below.

In previous studies [16,22,23], the dynamic contact lines are treated by modifying the surface tension component of the interfacial boundary condition in the cell adjacent to the wall. The contact angle is specified in the program input, and the contact line determined from the local fluid configuration. The surface force is then computed from the contact angle and the surface tension. In case of a static contact line, we compute the contact angle from the local fluid configuration and then apply the surface force in the same manner as these previous studies [16,22,23].

D. Viscous Component of Interfacial Boundary Condition

As mentioned above, the previous VOF techniques use a simplified boundary condition, Eq. (13), for the normal stress balance. To eliminate the assumption that the viscous terms in the interfacial boundary condition are negligible, we have included an option for computing the viscous forces. The local unit vector normal to the interface is computed in the manner used in [23] during surface tension computations. Once the coordinate axis most nearly normal to the interface has been determined, a local height function analogous to (3) is computed and the unit surface normal is obtained from (4).

Next, the components of the viscous stress tensor, (9), are computed using the provisional velocities, $\tilde{\mathbf{v}}_\ell^n$, where only velocities within the liquid phase are included in the finite difference formulas. For example, with reference to Figure 2, the components of the viscous stress tensor, assuming constant grid spacing, are computed as:

$$\tau_{xx} = 2\mu \frac{U_{i+1/2,j} - U_{i-1/2,j}}{\Delta x}, \tag{22a}$$

$$\tau_{yy} = 2\mu \frac{V_{i,j+1/2} - V_{i,j-1/2}}{\Delta y}, \tag{22b}$$

and $$\tau_{xy} = \tau_{yx} = \mu\left(\frac{U_{i+1/2,j} + U_{i-1/2,j} - U_{i+1/2,j-1} - U_{i+1/2,j-1}}{2\Delta y} + \frac{V_{i+1,j+1/2} - V_{i-1,j-1/2}}{2\Delta x}\right). \tag{22c}$$

With the viscous stress tensor and the unit normal vector available, the viscous component of the interfacial boundary condition is computed from $\mathbf{n}\cdot\boldsymbol{\tau}_\ell\cdot\mathbf{n}$.

E. Potential Flow in the Vapor Phase

As stated above, for stability problems such as flow of a thin liquid sheet, allowing the pressure in the vapor phase to vary is vital. We have implemented a method for solving the potential flow equation in the vapor phase which is coupled to the full NSE in the liquid phase through the interfacial conditions. This allows computation of the pressure in the vapor phase as a function of time and position.

With the assumptions that the vapor phase is inviscid, and the flow in the vapor phase is irrotational, the vapor phase may be modeled using potential flow,

$$\nabla^2\phi_v = 0, \tag{23}$$

where ϕ_v is the vapor phase potential. The pressure and velocities in the vapor phase are defined as

$$p_v = -\rho_v \frac{\partial \phi_v}{\partial t} \tag{24}$$

and $$\mathbf{v}_v = \nabla\phi_v. \tag{25}$$

Therefore, in the vapor phase, we must solve Laplace's equation on a region with curved boundaries having Neuman boundary conditions. This is accomplished using standard second order accurate finite difference formulas for (23) in the bulk of the vapor phase and adjacent to straight boundaries. At the interface between the two fluids, a more complex treatment is required.

We have implemented a modified form of a second order accurate method for solving Poisson's equation in a region with curved boundaries having mixed boundary conditions. Bramble and Hubbard [30] define a second order accurate operator,

$$\delta_n\phi_0 = \phi_0\sum_{i=1}^{3} a_i - \sum_{i=1}^{3} a_i\phi_i\,, \tag{26}$$

for the normal derivative using three points within the region of interest, where $\delta_n\phi_0$ is the normal derivative of ϕ_0 at the surface point of interest, ϕ_i are three points within the vapor phase, and the coefficients, a_i, are determined from solution of the system of equations:

$$\begin{bmatrix} \bar{y}_1 & \bar{y}_2 & \bar{y}_3 \\ \bar{x}_1 & \bar{x}_2 & \bar{x}_3 \\ \bar{x}_1^2 - \bar{y}_1^2 & \bar{x}_2^2 - \bar{y}_2^2 & \bar{x}_3^2 - \bar{y}_3^2 \end{bmatrix}\begin{bmatrix} a_1 \\ a_2 \\ a_3 \end{bmatrix} = \begin{bmatrix} 1 \\ 0 \\ 0 \end{bmatrix}, \tag{27}$$

where $\bar{y}_i$ and $\bar{x}_i$ are the distances from surface point of interest to the points ϕ_i in the normal and tangential directions, respectively. In addition, Bramble and Hubbard [30] present criteria which ensure that the operator yields a diagonally dominant system of equations.

The boundary condition for the vapor phase potential at the interface is conservation of the normal velocity, (10). Thus, the boundary operator is equal to the velocity normal velocity in the liquid phase plus a small correction arising from the derivation,

$$\delta_n\phi_0 = v_{\bar{y}} + \frac{\partial v_{\bar{y}}}{\partial \bar{x}}\sum_{i=1}^{3} a_i\bar{x}_i\bar{y}_i\,, \tag{28}$$

where $v_{\bar{y}}$ is the normal velocity at the interface and $\partial v_{\bar{y}}/\partial\bar{x}$ is the tangential derivative of the normal velocity at the interface [30]. The value of the vapor phase potential at the interface, needed to solve Laplace's equation, can be obtained by combining (27) and (28) and rearranging to yield

$$\phi_0 = \frac{v_{\bar{y}} + \frac{\partial v_{\bar{y}}}{\partial \bar{x}} \sum_{i=1}^{3} a_i \bar{x}_i \bar{y}_i + \sum_{i=1}^{3} a_i \phi_i}{\sum_{i=1}^{3} a_i}. \tag{29}$$

As stated above, since we have assumed the vapor phase to be inviscid, no restrictions are placed on the tangential velocity at the interface.

Incorporation of the liquid phase viscous terms and variations in the vapor phase pressure in the interfacial boundary condition, yield the following solution procedure. First, compute the surface curvature from the local liquid configuration. Next, compute the surface normal velocity from the change in surface position and solve (23) for the vapor phase potential. Third, compute the vapor phase pressure from (24). Then, compute the explicit guess for the liquid phase velocity field from (14). Fifth, compute the interfacial liquid phase stress from (9). Sixth, compute the pressure on the liquid side of the interface from (13). Next, solve the Poisson pressure equation, (16), to yield the new liquid phase pressure field. Then, update the liquid phase velocity field using (15). Finally, solve (12) to yield the new fluid configuration.

This procedure may be repeated until the desired time is reached. The second and third steps have been added to allow for variations in the vapor phase pressure, while the fifth step is required for inclusion of the vapor phase viscous terms in the interfacial conditions.

III. NUMERICAL RESULTS

In this section we present results from three sample problems chosen to demonstrate the accuracy of each of the major extensions to the VOF family of programs. First, we present results for flow in a lid-driven cavity which demonstrates the accuracy of the convective term differencing schemes. Then, we give examples of the die-swell

phenomenon where the liquid phase viscous component of the interfacial boundary condition is important. Finally, we present results from study of the stability of a thin liquid sheet flowing through an inviscid vapor phase.

A. Flow in a Lid Driven Cavity

The lid-driven cavity (LDC) problem is commonly used for testing numerical solutions of the NSE. We have chosen to use a square cavity (Fig. 3), at $Re = HV/\nu = 1000$ and having an aspect ratio = $H/W = 1$, to test the accuracy of SOLA differencing with $\alpha = 0.5$ and the three third order accurate techniques described above.

Two computational grids were used for each differencing scheme, the first having 40 equally spaced cells in each direction and the second having cell spacings one half the mean spacing adjacent to the walls and twice the mean spacing in the center of the cavity. Results of these eight simulations, with the results of Ghia et al. [31] included for comparison, are presented in figure 4 for the horizontal component of velocity along the vertical centerline, AB, and in figure 5 for the vertical component of velocity along the horizontal centerline, CD.

The accuracy in predicting the local extrema in figures 4 and 5 for each case as compared to the results of Ghia et al. [31] are presented in Table I. Using variable grid spacing, we were able to get within 5% of the result of Ghia et al. while using only 10% as many computational cells.

Convective terms differencing scheme	Grid	
	Constant	Variable
SOLA ($\alpha = 0.5$)	54.3 %	38.8 %
QUICK	15.4 %	4.8 %
Third order accurate upwind	13.0 %	4.2 %
Kawamura and Kuwahara	12.4 %	6.7 %

Table I. Error for the lid driven cavity problem at Re=1000.

Any of the third order accurate methods produce markedly superior results to SOLA differencing for this problem; however, all of the third order cases required longer computation times. While KANDK yielded the most accurate results for the constant grid, the accuracy of this method was the worst of the third order accurate techniques for the variable grid. This difference in ranking is attributed to the inaccuracies present in the variable grid formulation of Kawamura and Kuwahara's [29] method as outlined in the appendix.

B. The Cartesian Die-Swell Problem

We have studied the Cartesian die-swell problem (figure 6) both with and without surface tension to test accuracy of the computation of the liquid phase viscous stress at the interface. Relatively minor additions were necessary to modify the surface tension algorithm in [23] to allow computation of the surface curvature for problems in Cartesian coordinates. Additional modifications in the velocity boundary conditions at the corner of the die were implemented in a manner analogous to that used by Hill [13,14]. The details of these changes can be found in Ref. [25].

Results from a die-swell case without surface tension at $Re = HV/\nu = 300$ and $Ca^{-1} = \sigma/V\mu = 0$, where V is the average inlet velocity. As shown in Figure 7a, the initial condition consisted of the free surface even with the edge of the die. The initial velocity profile was parabolic throughout the liquid phase and the liquid phase viscous component of the interfacial boundary condition was included. Figures 7b, 7c, 7d, and 7e show the evolution of the solution as a function of time until a steady state solution was obtained.

The predicted die-swell for the case with $Re = 300$ and $Ca^{-1} = 0$ are -15.66%. This is in good agreement with results from the literature of -15.24% [32] and -15.52% [33]. Results from several solutions using different computational grids are presented in

Table II. All simulations used an entrance zone within the die of 3.5H and had varying domain lengths as indicated, and the computation grid was graded with the minimum cell spacing in each direction adjacent to the static contact line.

		Minimum Cell Spacing			
		0.04H	0.03H	0.02H	0.01H
Domain Length	20H	−14.48%	−14.92%	−15.20%	−15.12%
	25H	−14.78%	−15.08%	−15.52%	−15.37%
	30H	−15.05%	−15.14%	−15.62%	−15.53%
	35H	−15.19%	−15.17%	−15.66%	−15.63%
	40H	−15.31%	−15.21%	−15.66%	−15.67%

Table II. Results of solutions of the die-swell problem at Re = 300 and $Ca^{-1} = 0$.

Results of a similar series of solutions obtained for a case with surface tension at Re = 75 and $Ca^{-1} = 2$ are presented in Table III. In this case, the accuracy of the solution was improved by increasing the number of computational cells in the direction perpendicular to the flow direction and refining the grid in the region adjacent to the corner of the die. The predicted die swell shows more scatter than the previous case, but remains in reasonable agreement with the literature results of -11.16% [32], -10.92% [34], and -10.48% [33].

		Minimum Cell Spacing			
		0.0333	0.0278	0.0222	0.0167
Y-Direction Computational Cells	30	-10.99%	-11.61%	-11.38%	-11.26%
	36	***	-11.62%	-11.43%	-11.53%
	45	***	***	-10.91%	-11.37%
	60	***	***	***	-11.05%

*** combination not possible

Table III. Results of solutions of the die-swell problem at Re = 75 and $Ca^{-1} = 2$.

C. Stability of a Two-Dimensional Viscous Liquid Sheet

The final test problem presented results from the study of the stability of a thin liquid sheet of fluid flowing through an inviscid vapor phase. Figure 8 presents a diagram of the problem. The variation in the surface position, ε, shown in Figure 8 is assumed to be of the form

$$\varepsilon = \varepsilon_0 e^{\omega t + ikx} \tag{30}$$

where ε_0 is the initial amplitude, $\omega = \omega_r + i\omega_i$ is the complex growth rate, $i = (-1)^{1/2}$, and k is the wavenumber of the disturbance. Study using a linear stability analysis [24] yields dispersion relations for antisymmetric,

$$\begin{aligned} 0 = &\left(\tilde{\omega}_1 + 4\omega^2 Z\right)\tilde{\omega}_1 \tanh(m) \\ &+4m^3 Z^2\left[m\tanh(m) + \left(m^2 + \tilde{\omega}_1/Z\right)^{1/2}\tanh\left(\left(m^2 + \tilde{\omega}_1/Z\right)^{1/2}\right)\right] + \tilde{\rho}\tilde{\omega}^2 + m^3, \end{aligned} \tag{31}$$

and axisymmetric,

$$\begin{aligned} 0 = &\left(\tilde{\omega}_1 + 4\omega^2 Z\right)\tilde{\omega}_1 \coth(m) \\ &+4m^3 Z^2\left[m\coth(m) + \left(m^2 + \tilde{\omega}_1/Z\right)^{1/2}\coth\left(\left(m^2 + \tilde{\omega}_1/Z\right)^{1/2}\right)\right] + \tilde{\rho}\tilde{\omega}^2 + m^3, \end{aligned} \tag{32}$$

disturbances. Where $\tilde{\omega} = \tilde{\omega}_r + i\,We_\ell^{1/2}\tilde{\omega}_i$, $\tilde{\omega}_1 = \tilde{\omega} + i\,We_\ell^{1/2}m$, $\tilde{\omega}_r = \omega_r\left(\sigma/\rho_\ell a^3\right)^{-1/2}$, $\tilde{\omega}_i = \omega_i\left(a/U_0\right)m$, a is the initial sheet half-thickness, m=ka is the dimensionless wavenumber, and U_0 is the initial sheet velocity. The remaining parameters are defined as the Weber number, $We_\ell = \rho_\ell U_0^2 a/\sigma$, the Ohnesorge number, $Z = \mu_\ell\left(\rho_\ell a\sigma\right)^{-1/2}$, the density ratio, $\tilde{\rho} = \rho_g/\rho_\ell$.

It is possible to solve the dispersion relations, (31) and (32), for a given We_ℓ, Z and $\tilde{\rho}$ to yield the complex growth rate, $\tilde{\omega}$, as a function of the wave number. The real part of $\tilde{\omega}$ is dimensionless growth rate of a disturbance with wavenumber m. Results for a case We_ℓ=40, Z=0.1, and $\tilde{\rho}$=0.1 are shown in Figure 9 for both antisymmetric and axisymmetric disturbances represented by solid and dashed lines, respectively. The data

points plotted on Figure 9 represent our computed results for antisymmetric and axisymmetric disturbances represented by filled and open circles, respectively.

Solutions at m=1 were obtained on a computational domain with $2\pi a$ in the primary direction of flow and 8a perpendicular to the flow. This problem was discretized on a computational grid with 360 cells constantly spaced cells in the direction of flow and 100 graded cells perpendicular to the primary direction of flow. The grading was done so that a region of constant cell spacing was maintained adjacent to the interfaces. Problems with larger wavenumbers used the same computational grid with a shorter computational domain, keeping the number of computational cells per wave constant.

CONCLUSIONS

We have presented several extensions to the VOF method for tracking the location of the interface between a liquid and a vapor phase included in the SOLA method for solving the NSE. These have included more accurate methods for treating the convective terms in the NSE, a method for treating a static contact line, inclusion of the liquid phase viscous terms in the interfacial conditions, and the ability to solve for flow in the vapor phase coupled with the flow in the liquid phase.

These modifications allow the VOF technique to be applied to a wider variety of problems including the die-swell problem and study of the stability of a thin viscous sheet flowing through an inviscid vapor phase. We have shown that when the complete boundary condition at the interface between a viscous liquid and an inviscid liquid are imposed, the VOF technique coupled with the SOLA algorithm can, in fact, yield accurate solutions for complex problems.

APPENDIX: DERIVATION OF VARIABLE GRID KAWAMURA AND KUWAHARA METHOD

We begin by reviewing the derivation of Kawamura and Kuwahara. This is followed by an attempt to directly reproduce their derivation scheme for a variable grid. Finally, we will present our approximation of the variable grid KANDK method. For simplicity these derivations will be carried out using the points $u_{i+2}, u_{i+1}, u_i, u_{i-1}$, and u_{i-2} rather than the points at the cell faces used earlier and the constant grid spacing will be denoted h.

Kawamura and Kuwahara's Derivation

We begin with a second order upwind differencing scheme,

$$\left(u\frac{\partial u}{\partial x}\right)_i = \frac{u_i}{2h}\left(3u_i - 4u_{i-1} + u_{i-2}\right) \quad u_i > 0 \tag{A1a}$$

and

$$\left(u\frac{\partial u}{\partial x}\right)_i = \frac{u_i}{2h}\left(-u_{i+2} + 4u_{i+1} - 3u_i\right) \quad u_i < 0. \tag{A1b}$$

These formulas can be combined to yield a single formula independent of the flow direction

$$\begin{aligned}\left(u\frac{\partial u}{\partial x}\right)_i = {} & \frac{u_i}{4h}\left(-u_{i+2} + 4u_{i+1} - 4u_{i-1} + u_{i-2}\right) \\ & + \frac{|u_i|}{4h}\left(u_{i+2} - 4u_{i+1} + 6u_i - 4u_{i-1} + u_{i-2}\right).\end{aligned} \tag{A2}$$

From Taylor series expansions, this formula can be rewritten as

$$\left(u\frac{\partial u}{\partial x}\right)_i = u_i\left[\frac{\partial u}{\partial x} - \frac{h^2}{2}\frac{\partial^3 u}{\partial x^3} + O\left(h^4\right)\right] + |u_i|\left[h^3\frac{\partial^4 u}{\partial x^4} + O\left(h^5\right)\right]. \tag{A3}$$

Thus, the leading error in (A1) or (A2) can be reduced by eliminating the term

$$\frac{h^2}{2}\frac{\partial^3 u}{\partial x^3}. \tag{A4}$$

Improved accuracy is obtained by replacing the first term in (A3),

$$\frac{\partial u}{\partial x} - \frac{h^2}{2}\frac{\partial^3 u}{\partial x^3} + O(h^4), \tag{A5}$$

with

$$\frac{\partial u}{\partial x} + O(h^4) = \frac{-u_{i+2} + 8u_{i+1} - 8u_{i-1} + u_{i-2}}{12h}, \tag{A6}$$

yielding

$$\left(u\frac{\partial u}{\partial x}\right)_i = u_i\left[\frac{\partial u}{\partial x} + O(h^4)\right] + |u_i|\left[h^3\frac{\partial^4 u}{\partial x^4} + O(h^5)\right]. \tag{A7}$$

The resulting analogue of (A2) with an error of $O(h^4)$ is

$$\begin{aligned}\left(u\frac{\partial u}{\partial x}\right)_i &= \frac{u_i}{12h}(-u_{i+2} + 8u_{i+1} - 8u_{i-1} + u_{i-2}) \\ &\quad + \frac{|u_i|}{4h}(u_{i+2} - 4u_{i+1} + 6u_i - 4u_{i-1} + u_{i-2}).\end{aligned} \tag{A8}$$

Attempt at Kawamura and Kuwahara's Derivation with Variable Grid

In this section, we follow the steps of Kawamura and Kuwahara's derivation as far as possible for a variable grid. All derivations will be with respect to the dimensions shown in figure A1.

For a variable grid, (A1) becomes

$$\left(u\frac{\partial u}{\partial x}\right)_i = u_i\left(\frac{a+2b}{b(a+b)}u_i - \frac{a+b}{ab}u_{i-1} + \frac{b}{a(a+b)}u_{i-2}\right) \qquad u_i > 0 \tag{A9a}$$

and

$$\left(u\frac{\partial u}{\partial x}\right)_i = u_i\left(-\frac{c}{d(c+d)}u_{i+2} + \frac{c+d}{cd}u_{i+1} - \frac{2c+d}{c(c+d)}u_i\right) \qquad u_i < 0. \tag{A9b}$$

Thus, (A2) can be rewritten as

$$\left(u\frac{\partial u}{\partial x}\right)_i = \frac{u_i}{2}\left[-\frac{c}{d(c+d)}u_{i+2} + \frac{c+d}{cd}u_{i+1} + \left(-\frac{2c+d}{c(c+d)} + \frac{a+2b}{b(a+b)}\right)u_i \right.$$
$$\left. -\frac{a+b}{ab}u_{i-1} + \frac{b}{a(a+b)}u_{i-2}\right] + \frac{|u_i|}{2}\left[\frac{c}{d(c+d)}u_{i+2} - \frac{c+d}{cd}u_{i+1}\right. \qquad \text{(A10)}$$
$$\left. +\left(\frac{2c+d}{c(c+d)} + \frac{a+2b}{b(a+b)}\right)u_i - \frac{a+b}{ab}u_{i-1} + \frac{b}{a(a+b)}u_{i-2}\right].$$

In order to continue with Kawamura and Kuwahara's derivation, we begin by defining the terms in A3.

$$\frac{\partial u}{\partial x} + O(h^2) = \left[\frac{b}{c(b+c)}u_{i+1} + \frac{c-b}{bc}u_i - \frac{c}{b(b+c)}u_{i-1}\right], \qquad \text{(A11)}$$

$$\frac{\partial^3 u}{\partial x^3} + O(h^4) = \left[\frac{6(a+2b-c)}{d(c+d)(b+c+d)(a+b+c+d)}(u_{i+2} - u_i)\right.$$
$$-\frac{6(a+2b-c-d)}{cd(a+b+c)(b+c)}(u_{i+1} - u_i) + \frac{6(d+2c-b-a)}{ab(b+c+d)(b+c)}(u_{i-1} - u_i)$$
$$\left. -\frac{6(d+2c-b)}{a(a+b)(a+b+c)(a+b+c+d)}(u_{i-2} - u_i)\right], \qquad \text{(A12)}$$

and $$\frac{\partial^4 u}{\partial x^4} + O(h^5) = \frac{24}{d(c+d)(b+c+d)(a+b+c+d)}(u_{i+2} - u_i)$$
$$-\frac{24}{cd(a+b+c)(b+c)}(u_{i+1} - u_i) - \frac{24}{ab(b+c+d)(b+c)}(u_{i-1} - u_i)$$
$$+\frac{24}{a(a+b)(a+b+c)(a+b+c+d)}(u_{i-2} - u_i). \qquad \text{(A13)}$$

When (A11), (A12), and (A13) are substituted into (A3), it does not yield (A2), implying that the derivation of Kawamura and Kuwahara's method is inaccurate for variable grids.

Approximate Kawamura and Kuwahara Derivation with Variable Grid

We can obtain an approximate form of Kawamura and Kuwahara's technique by beginning the derivation with (A7). After substituting the variable grid analogue of (A6),

$$\frac{\partial u}{\partial x}+O(h^4)=-\frac{bc(a+b)}{d(c+d)(b+c+d)(a+b+c+d)}(u_{i+2}-u_i)$$
$$+\frac{b(a+b)(c+d)}{cd(a+b+c)(b+c)}(u_{i+1}-u_i)-\frac{c(a+b))(c+d)}{ab(b+c+d)(b+c)}(u_{i-1}-u_i)$$
$$+\frac{bc(c+d)}{a(a+b)(a+b+c)(a+b+c+d)}(u_{i-2}-u_i), \qquad \text{(A14)}$$

and (A13) into (A7) the resulting approximate formula for Kawamura and Kuwahara's method on a variable grid becomes

$$\left(u\frac{\partial u}{\partial x}\right)_i=\frac{-bc(a+b)\,u_i+24|u_i|}{d(c+d)(b+c+d)(a+b+c+d)}(u_{i+2}-u_i)$$
$$+\frac{b(a+b)(c+d)\,u_i-24|u_i|}{cd(a+b+c)(b+c)}(u_{i+1}-u_i)$$
$$-\frac{c(a+b))(c+d)\,u_i-24|u_i|}{ab(b+c+d)(b+c)}(u_{i-1}-u_i)$$
$$+\frac{bc(c+d)\,u_i+24|u_i|}{a(a+b)(a+b+c)(a+b+c+d)}(u_{i-2}-u_i). \qquad \text{(A15)}$$

ACKNOWLEDGMENTS

This study is supported by industrial contributions and the National Science Foundation under grant CTS-9258667. The computations are conducted, in part, using the Cornell National Supercomputer Center, a resource of the Center for Theory and Simulation in Science and Engineering at Cornell University, which is funded in part by the National Science Foundation, New York State, and the IBM Corporation. Portions of this work were used by J.F.M. as partial fulfillment of the requirements for the Ph.D. degree at the Institute of Paper Science and Technology.

REFERENCES

1. J. M Floryan and H. Rasmussen, Numerical methods for viscous flows with moving boundaries, *Appl. Mech. Rev.*, **42**, 323 (1989).

2. C. W. Hirt, , J. L. Cook, and T. D. Butler, A Lagrangian method for calculating the dynamics of an incompressible fluid with free surface, *J. Comput. Phys.*, **5**, 103 (1970).

3. W. P. Crowley, "FLAG: A free-Lagrangian method for numerically simulating hydrodynamic flows in two dimensions," *Lecture Notes in Physics*, **8**, Springer-Verlag, New York, 37 (1971).

4. W. P. Crowley, "Free Lagrangian methods for compressible flows in two space dimensions," *Lecture Notes in Physics*, **238**, Springer-Verlag, New York, 1 (1985).

5. M. J. Fritts and J. P. Boris, "The Lagrangian solution of the transient problems in hydrodynamics using a triangular mesh," *J. Comput. Phys.*, **31**, 173 (1979).

6. M. J. Fritts, W. P. Crowley, and E. H. Trease Eds., *The free Lagrange method, Lecture Notes in Physics*, **238**, Springer-Verlag, New York, (1985).

7. C. W. Hirt, A. A. Amsden, and J. L. Cook, An arbitrary Lagrangian-Eulerian computing method for all speeds, *J. Comput Phys.*, **14**, 227 (1974).

8. A. A. Amsden, H. M. Ruppel, and C. W. Hirt, "SALE: A simplified ALE computer program for fluid flow at all speeds," LA-8095, Los Alamos National Laboratory, 1980 (unpublished).

9. F. L. Addesio, D. E. Carroll, J. K. Dukowicz, F. H. Harlow, J. N. Johnson, B. A. Kashiwa, M. E. Maltrud, and H. M .Ruppel, "CAVEAT: A computer code for fluid dynamics problems with large distortion and internal slip," LA-10613-MS, Los Alamos National Laboratory, 1986 (unpublished).

10. P. Bach and D. Hassager, An algorithm for the use of the Lagrangian specification in Newtonian fluid mechanics and applications to free-surface flow, *J. Fluid Mech.*, **152**, 173 (1985).

11. B. D. Nichols and C. W. Hirt, Calculating three-dimensional free surface flows in the vicinity of submerged and exposed structures, *J. Comput. Phys.*, **12**, 234 (1973).

12. B. D. Nichols and C. W. Hirt, Improved free surface boundary conditions for numerical incompressible-flow calculations, *J. Comput. Phys.*, **8**, 434 (1971).

13. G. A. Hill, "Numerical simulation of free surface flows," Doctoral Dissertation, University of Saskatchewan, Saskatoon (1979).

14. G. A. Hill, C. A. Shook, and M. N. Esmail, Finite difference simulation of die swell for a Newtonian Fluid, *Canadian J. Chem. Eng.*, **59**, 100 (1981).

15. F. H. Harlow and J. E. Welch, Numerical calculation of time-dependent viscous incompressible flow of fluid with free surface, *Phys. Fluids*, **8**, 2182 (1965).

16. C. W. Hirt and B. D. Nichols, Volume of fluid (VOF) method for the dynamics of free boundaries, *J. of Comput. Phys.*, **39**, 201 (1981).

17. B. D. Nichols, C. W. Hirt, and R. S. Hotchkiss, "SOLA-VOF: A solution algorithm for transient fluid flow with multiple free boundary." LA-8355, Los Alamos National Laboratory, 1980 (unpublished).

18. W. F. Noh and P. Woodward, "SLIC (Simple Line Interface Calculation)," *Lecture Notes in Physics*, **59**, Springer-Verlag, New York, 330 (1976).

19. J. U. Brackbill, D. B. Kothe, and C. Zemach, A continuum method for modeling surface tension, *J. Comput. Phys.*, **100**, 335 (1992).

20. D. B. Kothe and R. C. Mjolsness, RIPPLE: A new method for incompressible flows with free surfaces, *AIAA J.*, **30**, 2694 (1992).

21. D. B. Kothe, R. C. Mjolsness, and M. D. Torrey, "RIPPLE: A computer program for incompressible flows with free surfaces," LA-12007-MS, Los Alamos National Laboratory, 1991 (unpublished).

22. M. D. Torrey, L. D. Cloutman, R. C. Mjolsness, and C. W. Hirt, "NASA-VOF2D: A computer program for incompressible flows with free surfaces." LA-10612-MS. Los Alamos National Laboratory, 1985 (unpublished).

23. M. D. Torrey, R. C. Mjolsness, and L. R. Stein, "NASA-VOF3D: A three-dimensional computer program for incompressible flows with free surfaces." LA-11009-MS, Los Alamos National Laboratory, 1987 (unpublished).

24. X. Li and R. S. Tankin, On the temporal instability of a two-dimensional viscous liquid sheet, *J. Fluid Mech.*, **226**, 425 (1991).

25. J. F. McKibben, "A computational fluid dynamics model for transient three-dimensional free surface flows," Doctoral Dissertation in progress, Institute of Paper Science and Technology, Atlanta, GA, (1993).

26. B. P. Leonard, A stable and accurate convective modeling procedure based on quadratic upstream interpolation, *Comput. Meth. Appl. Mech. Eng.*, **19**, 59 (1979).

27. C. J. Freitas, R. L. Street, A. N. Findikakis and J. R. Koseff, Numerical simulation of three-dimensional flow in a cavity, *Int. J. Num. Meth. Fluids*, **5**, 561 (1985).

28. R. K. Agarwal, "A third-order-accurate upwind scheme for Navier-Stokes solutions at high Reynolds numbers," AIAA Paper AIAA-81-0112, (1981).

29. T. Kawamura and K. Kuwahara, "Computation of high Reynolds number flow around a circular cylinder with surface roughness," AIAA Paper AIAA-84-0340, (1984).

30. J. H. Bramble and B. E. Hubbard, Approximation of solutions of mixed boundary value problems for Poisson's equation by finite differences, *J. Assoc. Comput. Mach.*, **12**, 114 (1965).

31. U. Ghia, K. N. Ghia and C. T. Shin, High-Re solutions for incompressible flow using the Navier-Stokes equations and a multigrid method. *J. Comput. Phys.*, **48**, 387 (1982).

32. Fluid Dynamics International Inc. FIDAP User's Manual, Evanston, IL, Rev. 5.0, 1st Edition, 6-1 (1990).

33. J. Omedei, Computer solutions of a plane Newtonian jet with surface tension, *Comput. Fluids*, **7**, 79 (1979).

34. F. Dupret, "A method for the computation of viscous flow by finite elements with free boundaries and surface tension," Finite Element Flow Analysis, Ed: T. Kawai, Univ. of Tokyo Press, Tokyo, 1982.

Figure 1. Schematic of computational grid geometry.

Figure 2. Example fluid configuration for viscous term computation.

Figure 3. Schematic of the lid-driven cavity problem.

Figure 4. Plots of the horizontal component of velocity along the vertical centerline
△ Ghia et al. [31], ——— variable grid, and - - - - - - constant grid.

Figure 5. Plots of the vertical component of velocity along the horizontal centerline
△ Ghia et al. [31], ——— variable grid, and - - - - - - constant grid.

Figure 6. Schematic of the die-swell problem.

Figure 7. Results from the die-swell problem at Re = 300 and $Ca^{-1} = 0$

Figure 8. Schematic of the sheet instability problem.

Figure 9. Non-dimensional growth rate for We_ℓ=40, Z=0.1, and $\tilde{\rho}$=0.1 obtained from numerical solution of the Li and Tankin's [24] dispersion relations. Open and closed circles represent results of our computational analysis.

Figure A1. Diagram of variable grid dimensions.

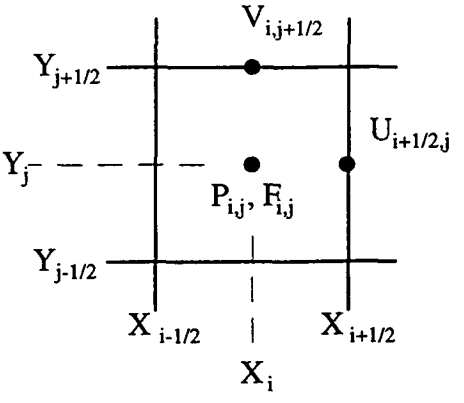

Figure 1

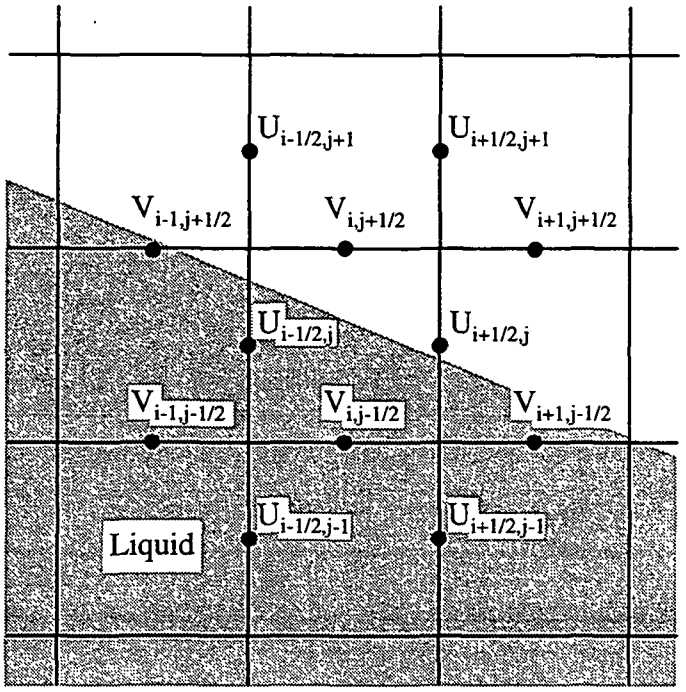
$U_{i-1/2,j+1}$
$U_{i+1/2,j+1}$
$V_{i-1,j+1/2}$
$V_{i,j+1/2}$
$V_{i+1,j+1/2}$
$U_{i-1/2,j}$
$U_{i+1/2,j}$
$V_{i-1,j-1/2}$
$V_{i,j-1/2}$
$V_{i+1,j-1/2}$
$U_{i-1/2,j-1}$
$U_{i+1/2,j-1}$
Liquid

Figure 2

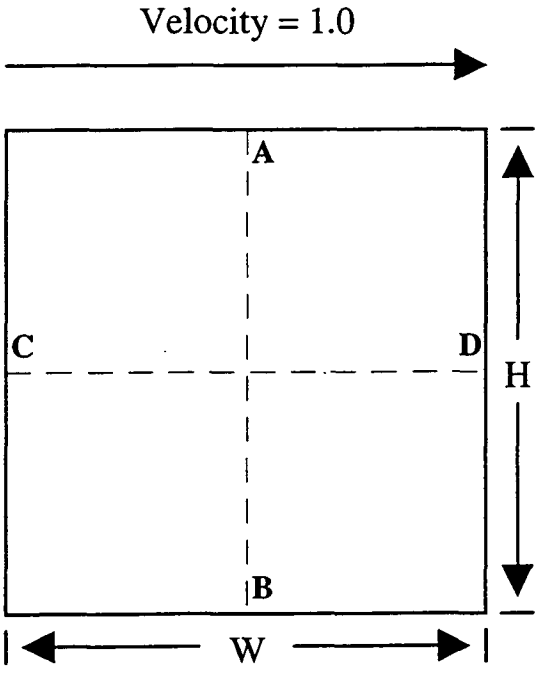

Figure 3

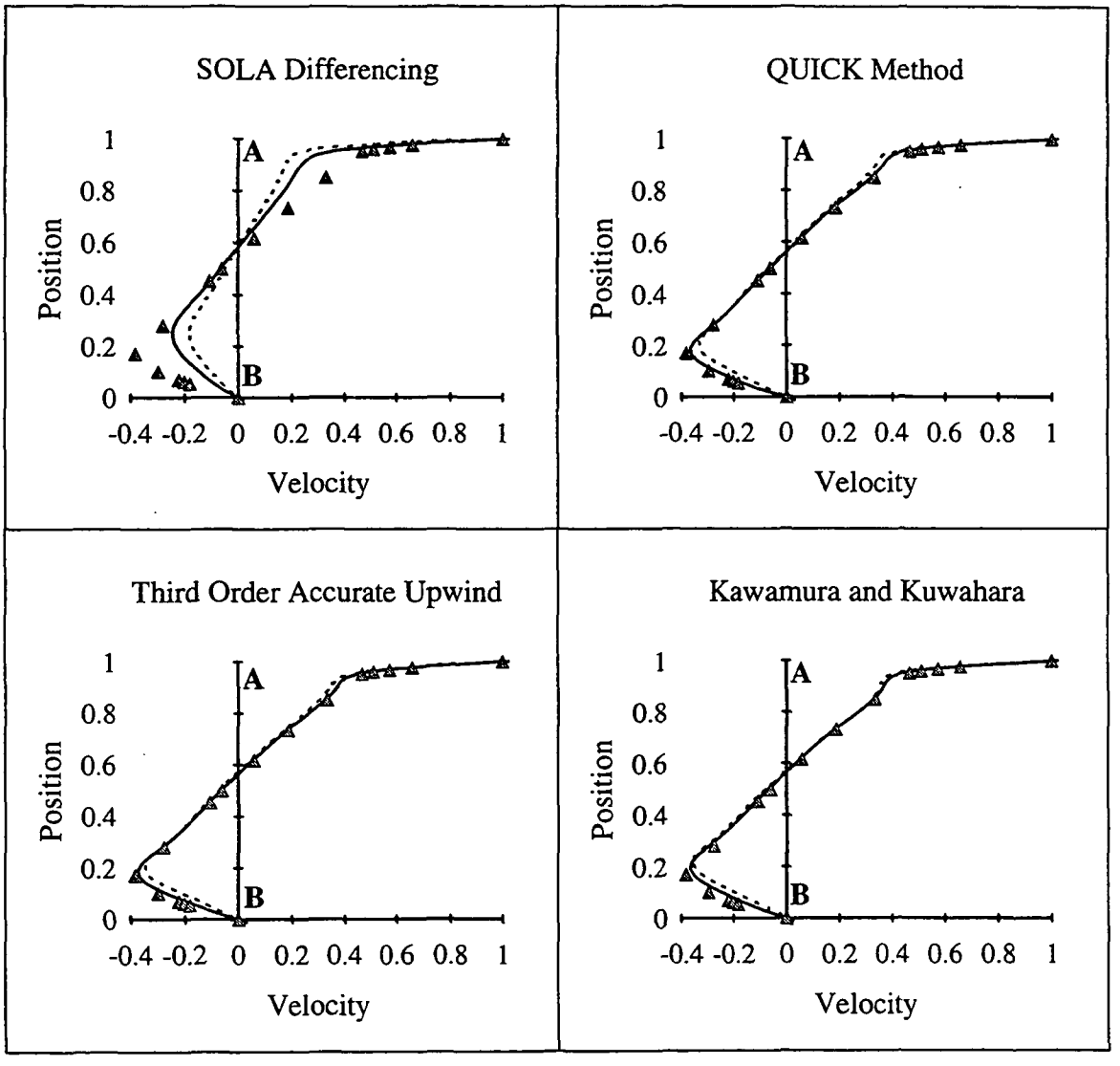
SOLA Differencing
QUICK Method
Third Order Accurate Upwind
Kawamura and Kuwahara
Position
Velocity
A
B
1
0.8
0.6
0.4
0.2
0
-0.4 -0.2 0 0.2 0.4 0.6 0.8 1

Figure 4

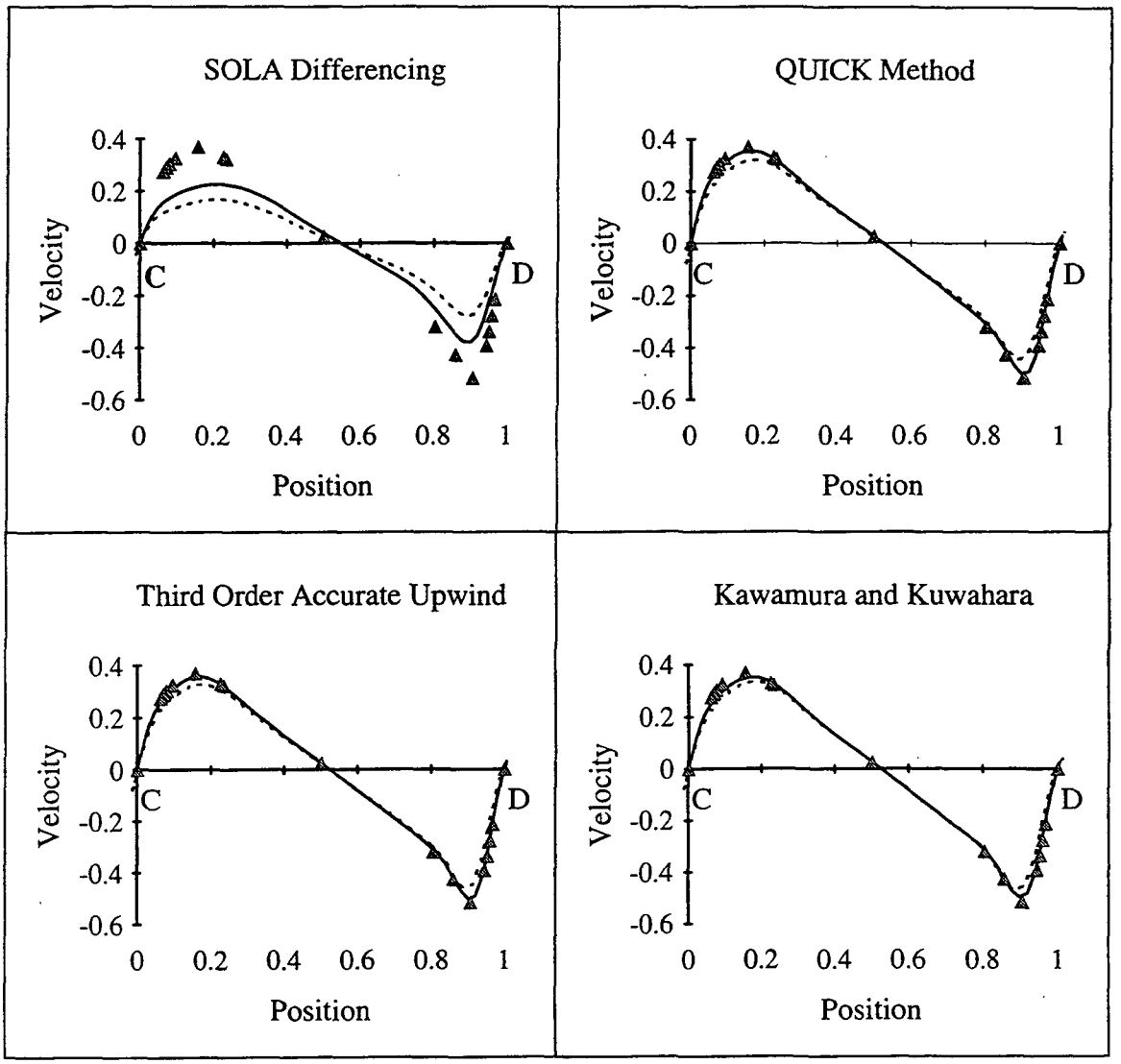
SOLA Differencing
QUICK Method
Third Order Accurate Upwind
Kawamura and Kuwahara
Velocity
Position
C
D
0.4
0.2
0
-0.2
-0.4
-0.6
0
0.2
0.4
0.6
0.8
1

Figure 5

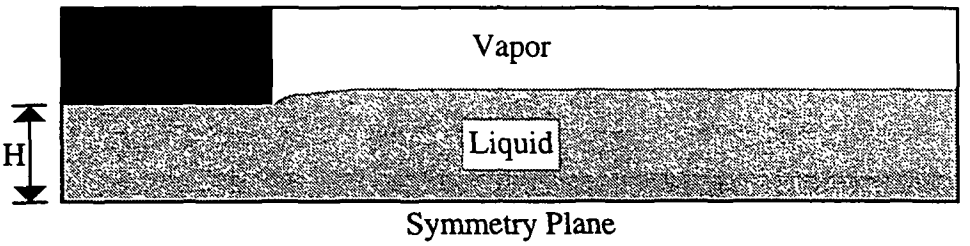

Figure 6

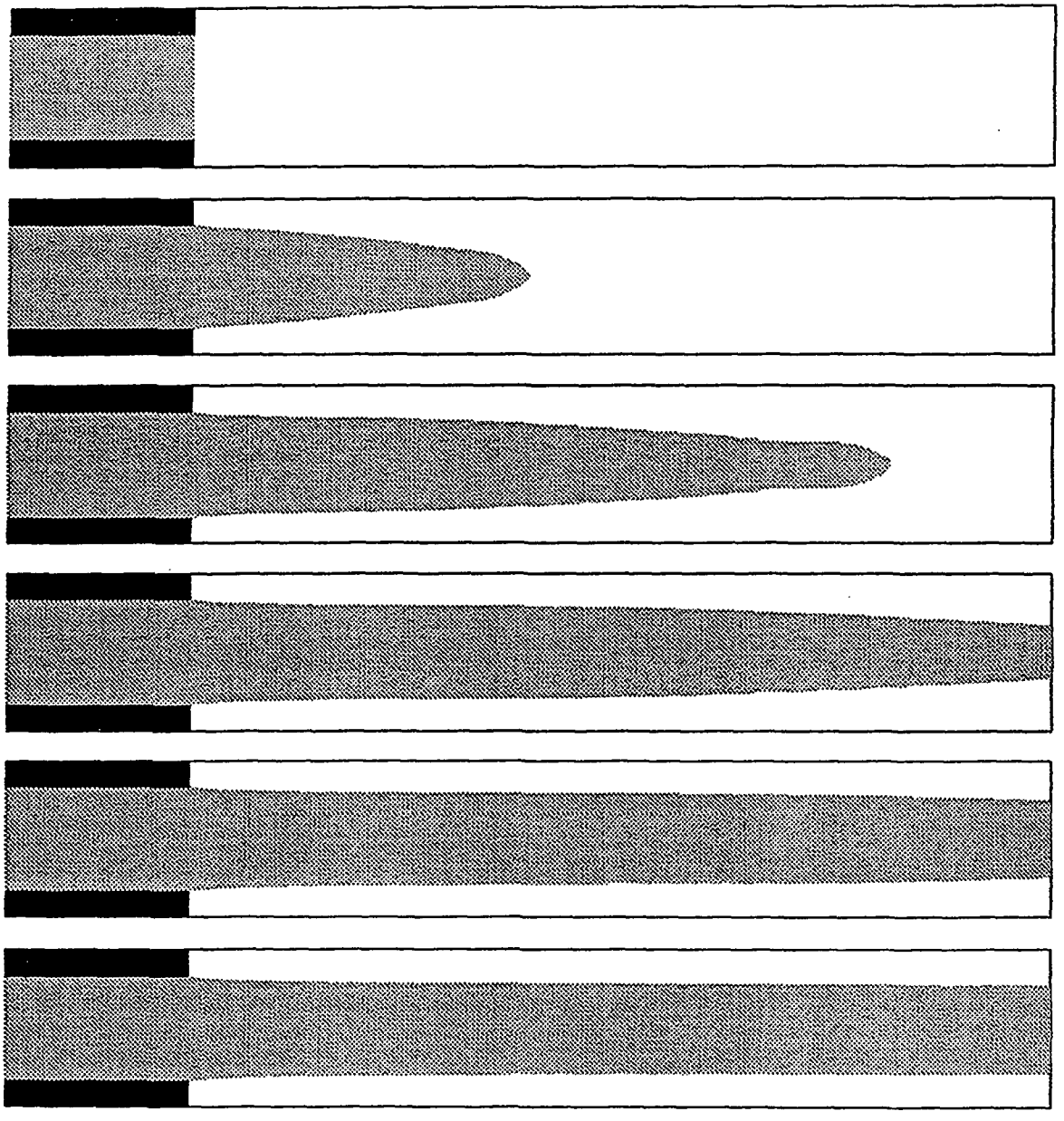

Figure 7

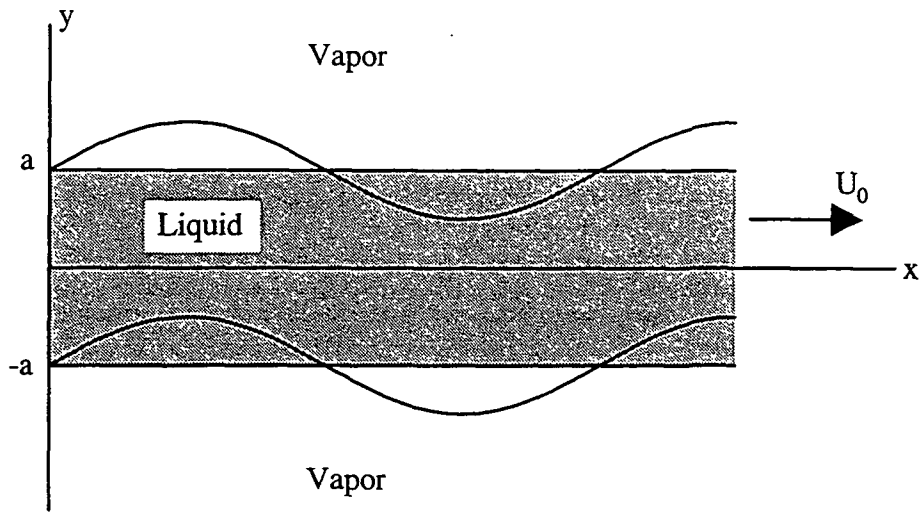

Figure 8

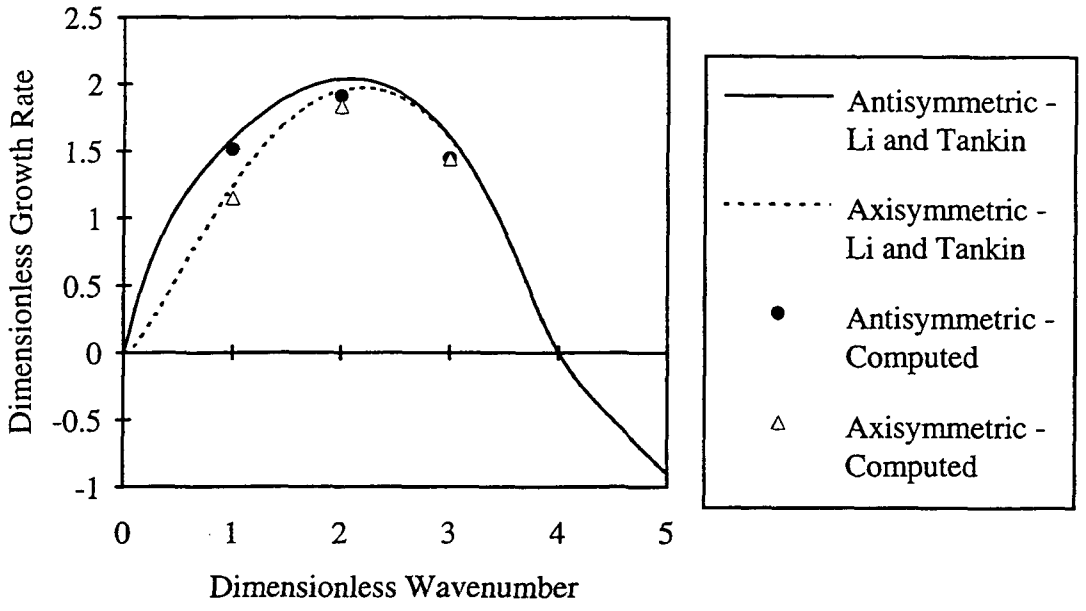
2.5
2
1.5
1
0.5
0
-0.5
-1
0
1
2
3
4
5
Dimensionless Growth Rate
Dimensionless Wavenumber
Antisymmetric - Li and Tankin
Axisymmetric - Li and Tankin
Antisymmetric - Computed
Axisymmetric - Computed

Figure 9

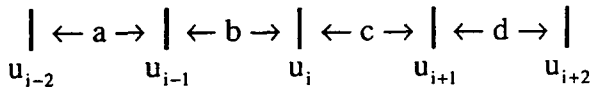

Figure A1